

Revisiting ^{129}Xe electric dipole moment measurements applying a new global phase fitting approach

Tianhao Liu^{1,2,a}, Katharina Rolfs^{1,b}, Isaac Fan¹, Sophia Haude¹, Wolfgang Kilian¹, Liyi Li², Allard Schnabel¹, Jens Voigt¹ and Lutz Trahms¹

¹ Physikalisch-Technische Bundesanstalt Berlin, 10587 Berlin, Germany

² Department of Electrical Engineering and Automation, Harbin Institute of Technology, 150001 Harbin, China

the date of receipt and acceptance should be inserted later

Abstract. By measuring the nuclear magnetic spin precession frequencies of polarized ^{129}Xe and ^3He , a new upper limit on the ^{129}Xe atomic electric dipole moment (EDM) $d_A(^{129}\text{Xe})$ was reported in Phys. Rev. Lett. 123, 143003 (2019). Here, we propose a new evaluation method based on global phase fitting (GPF) for analyzing the continuous phase development of the ^3He - ^{129}Xe comagnetometer signal. The Cramer-Rao Lower Bound on the ^{129}Xe EDM for the GPF method is theoretically derived and shows the potential benefit of our new approach. The robustness of the GPF method is verified with Monte-Carlo studies. By optimizing the analysis parameters and adding data that could not be analyzed with the former method, we obtain a result of $d_A(^{129}\text{Xe}) = 1.1 \pm 3.6$ (stat) ± 2.0 (syst) $\times 10^{-28}$ e cm in an unblinded analysis. For the systematic uncertainty analyses, we adopted all methods from the aforementioned PRL publication except the comagnetometer phase drift, which can be omitted using the GPF method. The updated null result can be interpreted as a new upper limit of $|d_A(^{129}\text{Xe})| < 8.3 \times 10^{-28}$ e cm at the 95% C.L.

PACS. XX.XX.XX No PACS code given

1 Introduction

A quantum field theory that models the formation of the imbalance of matter over antimatter in our universe must fulfill the Sakharov conditions [1]. One of those conditions is the \mathcal{CP} violation (\mathcal{C} is charge conjugation and \mathcal{P} is parity reversal). The best-tested standard model (SM) of particle physics provides two sources of \mathcal{CP} violation, the phase of the Cabibbo-Kobayashi-Maskawa matrix and the term $\bar{\theta}$ in the QCD Lagrangian [2]. However, the \mathcal{CP} violation within the SM is too small to produce the observed rate of the matter to antimatter asymmetry, motivating searches for physics beyond-the-SM (BSM). BSM theories generally include additional sources of \mathcal{CP} violation [2, 3], such as a larger permanent electric dipole moment (EDM) of fundamental or composite particles [4, 5]. So far, all measurement results of EDMs in more than ten diverse systems, with the first published in 1957 [6], are consistent with zero. These null results are interpreted as upper limits on EDMs and place constraints on various sources of \mathcal{CP} violation and masses of BSM particles, thus directing the search of BSM scenarios [7].

Long spin-coherence time and obtainable high polarization leading to high signal-to-noise ratios (SNR) make several diamagnetic systems such as the ^{199}Hg and ^{129}Xe atom promising candidates for EDM experiments. Over the last 40 years, significant progress was made in the determination of upper limits for EDMs of diamagnetic systems (see Fig. 1). At present, the ^{199}Hg atomic EDM measurement is the most sensitive, and its upper limit sets constraints to multiple sources of \mathcal{CP} violation [8]. Considering various potential contributions to an atomic EDM, an improved limit on other systems, like the ^{129}Xe EDM $d_A(^{129}\text{Xe})$, will tighten these constraints. The theoretical results for ^{129}Xe EDM are more accurate and reliable than those obtained for ^{199}Hg EDM, therefore ^{129}Xe has the potential to probe new physics [9].

Recently, new upper bounds on the ^{129}Xe EDM using ^3He comagnetometry and SQUID detection have been reported by a joint collaboration between the University of Michigan, the Technical University of Munich and the Physikalisch-Technische Bundesanstalt (PTB) [11] as well as another independent group with comparable sensitivities [15], which are about five times smaller than the previous limit set in 2001 [16]. One of the challenges in both

^a email:silasliutianhao@gmail.com

^b email:katharina.rolfs@ptb.de

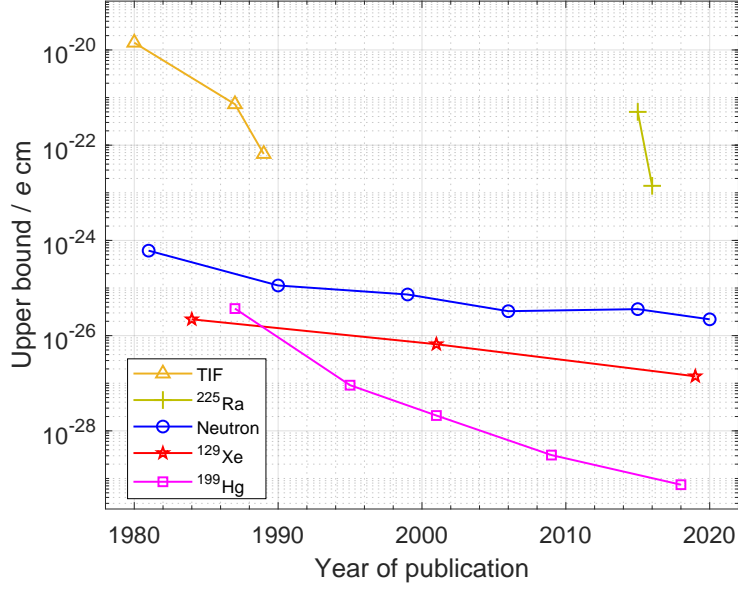


Fig. 1. Selected upper bounds of EDM of diamagnetic systems performed since 1980 at the 95% C.L. For all systems, the current upper bound has decreased more than an order of magnitude compared to their first published result [8, 10, 11, 12, 13, 14, 15, 16].

experiments is the comagnetometer frequency drift, which is several magnitudes larger than the expected frequency shift due to a potential ^{129}Xe EDM [17]. One approach to correct for the impact of the comagnetometer drift on the measured $d_A(^{129}\text{Xe})$ is using a deterministic physical model to fit the comagnetometer frequency drift [15, 18]. However, the physical origin of the comagnetometer frequency instability is subject of a controversial debate [19, 20], which was inspired by another theoretical model and motivated the performance of recent experiments to substantiate the former criticism [21, 22]. Instead, in Ref. [11] a phenomenological method was used, which does not need any physical model on the comagnetometer frequency drift, but a distinct pattern of electric fields with switching polarity. We will refer to that as the Pattern Combination (PC) method from here on.

Here, we propose a new analysis based on a Global Phase Fitting (GPF) method, where the EDM value is estimated by a single fit to the comagnetometer phase development within one complete measurement. Besides an experimentally deduced EDM function as used in Ref. [15], allowing to analyse any electric field pattern, our GPF method uses a polynomial function to account for the comagnetometer frequency drift. Sec. 2 gives a short description of the basic principle of measuring the ^{129}Xe EDM $d_A(^{129}\text{Xe})$ using comagnetometry. In addition, the PC method is introduced for comparison with the GPF method. The GPF method is elucidated in detail in Sec. 3, including the derivation of the Cramer-Rao Lower Bound (CRLB). The CRLB of the variance on the EDM value estimation using the GPF method is a factor of four smaller than that of the PC method. In Sec. 4 we validate the GPF method with Monte-Carlo simulations and compare the results of the PC and GPF method using the experimental data obtained for Ref. [11]. Eventually we recalculate the systematic uncertainties based on Ref. [11] and derive a new upper limit for the permanent ^{129}Xe EDM.

2 ^3He - ^{129}Xe -COMAGNETOMETRY

2.1 Basic principle

For ^{129}Xe atoms stored in a cell permeated by a uniform magnetic field \vec{B} and an electric field \vec{E} , that is parallel to \vec{B} , their nuclear spin precesses at an angular frequency

$$\omega_{\text{Xe}} = \left| \gamma_{\text{Xe}} B + \frac{d_A(^{129}\text{Xe}) E}{\hbar F_{\text{Xe}}} \right|, \quad (1)$$

where $F_{\text{Xe}} = 1/2$ is the total angular momentum number and γ_{Xe} is the gyromagnetic ratio of ^{129}Xe . The magnetic field B in Eq. (1) becomes an interference term for directly calculating $d_A(^{129}\text{Xe})$ from ω_{Xe} . To overcome the experimental

difficulties on controlling and measuring \vec{B} , comagnetometry was introduced with two collated species measured at the same time [16, 17, 23]. ^3He is an ideal candidate for comagnetometry due to its potentially high SNR and a negligible EDM compared to $d_A(^{129}\text{Xe})$ [24]. The weighted frequency difference between ^{129}Xe atoms and ^3He atoms is defined as

$$\omega_{\text{co}} = \omega_{\text{Xe}} - \frac{\gamma_{\text{Xe}}}{\gamma_{\text{He}}} \omega_{\text{He}}, \quad (2)$$

and commonly named the comagnetometer frequency. Here $\omega_{\text{He}} = |\gamma_{\text{He}} B|$ is the spin precession frequency of ^3He atoms with γ_{He} being its gyromagnetic ratio. Therefore, ω_{co} can be written as

$$\omega_{\text{co}} = \frac{2d_A(^{129}\text{Xe})}{\hbar} \vec{E} \cdot \hat{B}, \quad (3)$$

showing that ω_{co} is independent of the magnitude of the background magnetic field but depends on its orientation relative to the applied electric field. The current measurement sensitivity of ω_{co} is in the nHz range for a single measurement, while the comagnetometer frequency drift is at the μHz level, which causes a non-negligible systematic error [21, 22, 25]. Multiple physical models to describe the comagnetometer drift were proposed. The dominant terms thereby vary in different models. Furthermore, several parameters, such as the longitudinal relaxation time T_1 of the nuclear spins, used in these models are unknown or difficult to measure, making the frequency drift correction with a deterministic model inaccurate. By using a phenomenological model such as proposed here and in [11], these currently unsolved difficulties can be omitted.

2.2 Parameters of two measurement campaigns

The data used in our analysis were collected in the joint collaboration at the Berlin Magnetically Shielded Room (BMSR-2) facility at PTB Berlin. Table 1 summarizes the main experimental parameters of the two measurement campaigns carried out in 2017 and 2018, respectively. More details on the setup and process are given in Ref. [26]. The spin precession signal of the transverse magnetization of ^3He and ^{129}Xe was recorded by a dc-SQUID system with two channels (Z1,Z2). The high voltage and leakage current between the two electrodes of the cell were monitored. A background magnetic field B_0 in the range of 2.6 μT - 3 μT was applied to shift ω_{Xe} and ω_{He} to 30 Hz - 36 Hz and 90 Hz - 98 Hz, respectively, which are well above the vibrational interference signals (see Fig. 2). In order to further decrease the impact of the vibrational noise, a software SQUID gradiometer (Z1 - Z2) was used.

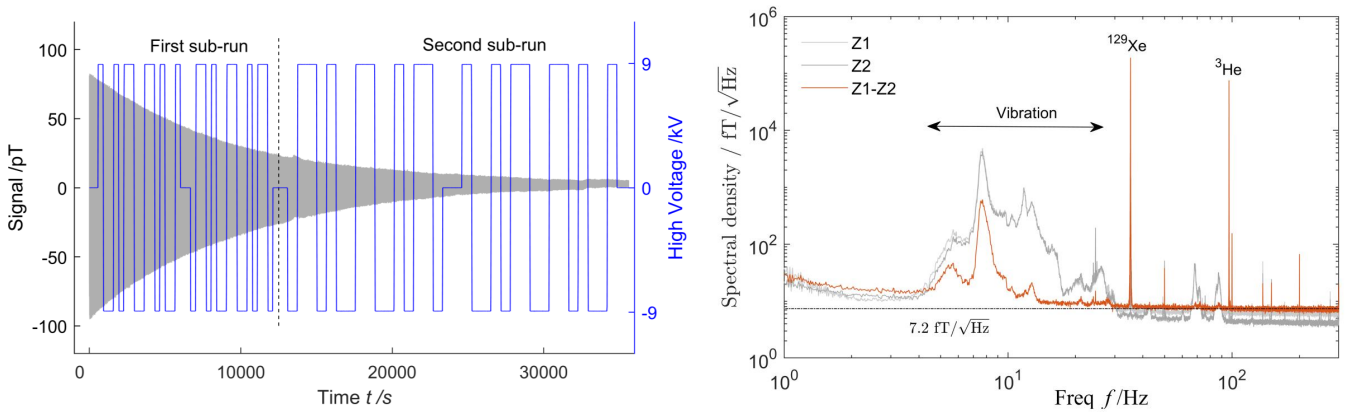


Fig. 2. Left: The SQUID gradiometer Z1 - Z2 signal (gray curve) and the modulated high voltage signal (blue line) of one run from the 2018 campaign. Right: The amplitude spectral density of data lasting 100 s from the starting of the first sub-run for two magnetometer channels (Z1 and Z2) and one software gradiometer (Z1 - Z2). The white noise level of the gradiometer is $\rho_\omega \approx 7.2 \text{ fT}/\sqrt{\text{Hz}}$. The variance of the white noise is $\sigma_\omega^2 = f_s \rho_\omega^2 / 2 = (154 \text{ fT})^2$, with the sampling frequency $f_s = 915.5245 \text{ Hz}$.

The left panel of Fig. 2 shows the raw SQUID gradiometer signal in pT (gray) of one run from the 2018 campaign lasting 35000 s exemplarily. This run comprises two so called sub-runs with 36 segments each. A segment is defined as the time of constant electric field. For the two sub-runs shown in Fig. 2, the segments last 300 s and 600 s, respectively. The first sub-run ranging from 50 s to 12400 s is used as an example in the data analysis section.

Table 1. Starting amplitude A_0 , transverse relaxation time T_2 , background magnetic field B_0 and segment length t_s of both measurement campaigns.

	2017	2018
$A_{0,\text{Xe}} / \text{pT}$	30-40	70-80
$A_{0,\text{He}} / \text{pT}$	4-5	20-25
$T_2^{\text{Xe}} / \text{s}$	6000-7000	8000-9000
$T_2^{\text{He}} / \text{s}$	7000-8000	8000-9000
$B_0 / \mu\text{T}$	2.6	3
t_s / s	400 or 800	100-800

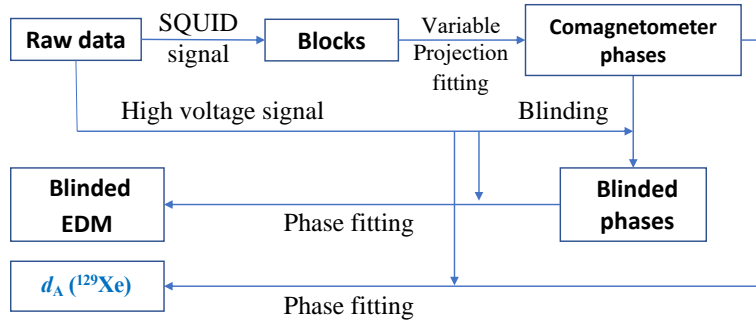
2.3 PC method

As mentioned above, one approach to mitigate the effect of the comagnetometer frequency drift is repetitively reversing the direction of the electric field \vec{E} . This allows to separate the impact of $d_A(^{129}\text{Xe})$ on ω_{co} from other interference terms. The E modulation method has been applied in diverse EDM experiments with varied modulation patterns [10, 14]. For the PC method, the common E pattern for one sub-run consists of 36 segments with an equal time interval t_s , and the sign of \vec{E} changes according to the following sequence $\pm[0 + - - + - + + - - + + - + - - + 0, 0 - + + - + - - + + - - + - + + - 0]$. The segments of zero voltage were added to allow for systematic error studies.

The PC method determines the EDM value from averaging the comagnetometer frequencies ω_{co} from 2^n ($n \in \mathbb{N}$) consecutive segments omitting those with zero voltages. This pattern is constructed to cancel the effect of the comagnetometer frequency drift up to $n - 1$ order when parametrized in polynomials. The effect of the higher order (above $n - 1$) drift dependency imposing a false EDM on each sub-run is deduced by applying polynomial fits to all ω_{co} within the sub-runs, leading to a correction for the EDM and an additional systematic uncertainty (for more details see Ref. [26]).

3 GLOBAL PHASE FITTING METHOD

The general data-processing procedure for the GPF method is illustrated in Fig. 3. For this method, the raw SQUID data of a sub-run is cut into continuous blocks of equal length. Each block data is fitted to deduce precession phases of both species ^3He and ^{129}Xe (see Sec. 3.1) and the continuous comagnetometer phase is derived for each block (see Sec. 3.2). For data blinding an additional phase, bound to the measured high voltage signal, can be added to the comagnetometer phase at this point (see Sec. 3.3). The EDM value is acquired by fitting the blinded comagnetometer phases using a polynomial function together with a constructed function comprising the phase evolution introduced by a hypothetical ^{129}Xe EDM. The unblinded EDM result is obtained by reanalyzing the raw comagnetometer phases, as illustrated in Fig. 3.

**Fig. 3.** The schematic process of the GPF method.

3.1 The phase of each block

The block length t_b is a free parameter with a suitable range from 1 s to 20 s, being short enough to exclude the amplitude decay and frequency drift, and long enough to perform the fit for our data [11]. The SQUID data in each

block are fitted to the function

$$y = a_{\text{Xe}} \sin(\omega_{\text{Xe}} t) + b_{\text{Xe}} \cos(\omega_{\text{Xe}} t) + a_{\text{He}} \sin(\omega_{\text{He}} t) + b_{\text{He}} \cos(\omega_{\text{He}} t) + a_i \sin(\omega_i t) + b_i \cos(\omega_i t) + c + d \cdot t, \quad (4)$$

where $a_{\text{Xe}/\text{He}/i}$, $b_{\text{Xe}/\text{He}/i}$, $\omega_{\text{Xe}/\text{He}}$, c , and d are the fit parameters and $\omega_{i=1,2,3,4} = 2\pi \times 50i \text{ s}^{-1}$ represent the power frequency and its harmonics. The constant and linear terms c and $d \cdot t$ describe the background magnetic field and its small drift as seen by the SQUID. The variable projection (VP) method is applied [27], where the nonlinear parameters $\omega_{\text{Xe}/\text{He}}$ are estimated separately from the linear parameters $a_{\text{Xe}/\text{He}/i}$, $b_{\text{Xe}/\text{He}/i}$, c , and d . To minimize the correlation between the fit terms in Eq. (4), the time of each block is assigned to be symmetrical around zero from $-t_b/2$ to $t_b/2$.

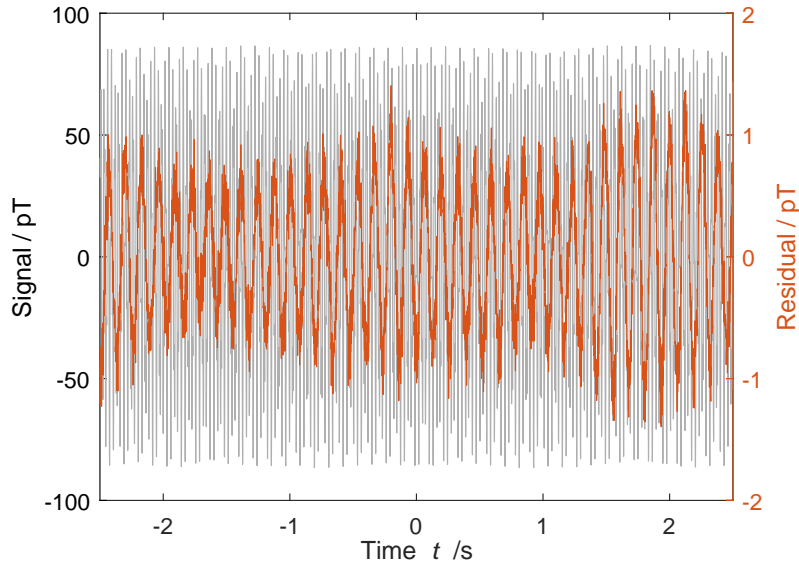


Fig. 4. The gradiometer signal (gray) for one block with $t_b = 5 \text{ s}$ and the residual of the fit (red).

Fig. 4 shows the raw SQUID data of a 5 s block from the start of the exemplary sub-run and the residual of the fit to this data. The residual is dominated by the mechanical vibration in the frequency range of 4 Hz - 25 Hz as shown in the right plot of Fig. 2. We can assume approximate orthogonality between the precession signal and the vibrational noise of our setup. Therefore, the error on the fit parameter values caused by the latter one is negligible compared to that caused by the white noise, although its integrated power is much larger than the white noise power. This was validated with Monte-Carlo simulations using the recorded vibrational noise (see Appendix A.1). The phase of each species for the block k in the range of $[-\pi, \pi)$ can be obtained by

$$\phi_m^k = \text{Arg}(a_m^k + i \cdot b_m^k), \quad (5)$$

where Arg is the function to get the principle argument of a complex number, i is the imaginary unit and $m = \text{Xe}$ or He . Note that due to the time centering, the estimated phase ϕ^k is referred to the middle time of each block $t_k = (k - 1/2)t_b$. The time interval of the block k is defined as (t_{k-1}, t_k) . The parameter uncertainties δa_m^k and δb_m^k are estimated from the covariance matrix of the fit

$$\text{Cov} = \frac{\vec{r}' \cdot \vec{r}}{\nu(\mathbf{J}' \cdot \mathbf{J})^{-1}}, \quad (6)$$

where \vec{r} is the residual, ν is the degrees of freedom and \mathbf{J} is the Jacobian matrix. The standard deviation of the derived phase $\delta\phi_{\text{Xe}/\text{He}}^k$ is

$$\delta\phi_m^k = \frac{\sqrt{(a_m^k \cdot \delta b_m^k)^2 + (b_m^k \cdot \delta a_m^k)^2 - 2a_m^k b_m^k \text{Cov}(a_m^k, b_m^k)}}{(a_m^k)^2 + (b_m^k)^2}. \quad (7)$$

Eq. (6) assumes that the residual \vec{r} stems from the wideband white noise, which is a conservative approach for our case since the main signal in the residuals is the narrowband vibrational noise, leading to an overestimation of the uncertainty $\delta\phi_m^k$. However, the ratio between $\delta\phi_m^k$ for different blocks reflects the decaying SNR. Therefore, these estimated uncertainties are used as weights in the subsequent GPF routine.

3.2 The accumulated comagnetometer phase

The accumulated phase Φ_m^k in a block k of the continuously precessing spins is the sum of the wrapped phase ϕ_m^k and a multiple of 2π

$$\Phi_m^k = \phi_m^k + 2\pi n_m^k, \quad (8)$$

where the integer n_m^k is determined as

$$n_m^k = \frac{\Phi_m^{k-1} + \omega_m^{k-1} t_b}{2\pi}, \quad (9)$$

rounded to the lower integer and $n_m^1 = 0$. Here, the frequencies ω_m^{k-1} are obtained by the fit of the block k using Eq. (4). If $\Phi_m^k - (\Phi_m^{k-1} + \omega_m^{k-1} t_b)$ is either $> \pi$ or $< -\pi$, n_m^k is incremented or decremented by one, respectively, to ensure a continuous phase evaluation. The standard deviation of the accumulated phase $\delta\Phi_m^k$ is equal to $\delta\phi_m^k$ as Eq. (8) does not introduce any additional uncertainty. According to Eq. (2), the evolved comagnetometer phase Φ_{co}^k for each block k is determined by

$$\Phi_{\text{co}}^k = \Phi_{\text{Xe}}^k - \frac{\gamma_{\text{Xe}}}{\gamma_{\text{He}}} \Phi_{\text{He}}^k. \quad (10)$$

3.3 The fitted EDM value

By integrating Eq. (3), the accumulated phase due to a hypothetical ^{129}Xe EDM d_h at the block k is

$$\Phi_{\text{EDM}}^k = t_b \frac{2d_h}{\hbar} \sum_{i=1}^k (\vec{E}_i \cdot \hat{B}), \quad (11)$$

where \vec{E}_i is the average electric field within the block i . By replacing d_h with a computer-generated pseudo-random EDM value d_{bias} , the bias phase Φ_{bias}^k is calculated and then used to blind the comagnetometer phase $\Phi_{\text{co,b}}^k = \Phi_{\text{co}}^k + \Phi_{\text{bias}}^k$ in order to avoid operator induced bias during process optimization. The value of d_{bias} has been saved in an independent file in a binary format and $\Phi_{\text{co,b}}^k$ was used for later data analysis.

The measured phase Φ_{co}^k originates not only from the potential ^{129}Xe EDM, but also from other sources such as chemical shift [21, 26]. These contributions are phenomenologically parametrized by a polynomial of g th order [28]. Hence, the comagnetometer phase is fitted with the function

$$\Phi_{\text{fit}}^k = a\Phi_{\text{EDM}}^k + p_0 + p_1\tilde{P}_1(t_k) + p_2\tilde{P}_2(t_k) + \dots + p_g\tilde{P}_g(t_k), \quad (12)$$

where $a, p_0, p_1, p_2, \dots, p_g$ are the global fit parameters. Here the time series t_k are normalized to the interval $[0,1]$ and shifted Legendre polynomials $\tilde{P}_n(t_k)$ are applied to decrease the correlation between polynomial coefficients [29]. The fit was conducted by using the iterative least squares estimation method with the built-in function *nlinfit* in MATLAB. Thereby the inverse values of the phase variances $(\delta\Phi_{\text{co}}^k)^2$ are used as weights. Fig. 5 shows the comagnetometer phase Φ_{co}^k , the fit phase Φ_{fit}^k , and the EDM function Φ_{EDM}^k constructed from the measured E -field pattern of the exemplary sub-run. To determine the order needed for the polynomial function in Eq. (12), we apply an F -test where the significance of adding q terms to the fitting function with g terms was evaluated by the integral probability

$$P_{g,g+q} = \int_0^{F_{g,g+q}} P_{\text{F}}(F; q, N - g - q) dF, \quad (13)$$

where P_{F} is the probability density function of the F -distribution and N is the number of data points [30]. The upper bound of the integral is

$$F_{g,g+q} = \frac{(N - g - q)(\chi_g^2 - \chi_{g+q}^2)}{q \cdot \chi_{g+q}^2}. \quad (14)$$

The order of the fit was defined sufficient when $P_{g,g+1}$ as well as $P_{g,g+2}$ are both smaller than a chosen threshold of P_{min} .

The atomic EDM of ^{129}Xe is calculated from the fit parameter a as

$$d_{\text{A}}(^{129}\text{Xe}) = a \cdot d_{\text{h}}. \quad (15)$$

The correlated uncertainties of the parameters are determined as the square root of the reciprocal of the diagonal of the covariance matrix, which inherently includes the uncertainty of the correlations between a and polynomial parameters. The influences of these correlations to the estimation of a are small due to the orthogonality between the

constructed function Φ_{EDM}^k and the polynomial function of the order up to $n - 2$ where 2^n is the number of nonzero high voltage segments. The correlation matrix for the exemplary sub-run (see Fig. 2) is given in Table 2. In this case, the correlations between the EDM parameter a and the polynomial coefficients are significantly smaller than 1, but nonzero, since the polynomials of higher than 3rd order are not orthogonal to Φ_{EDM}^k . The derived uncertainty is in good agreement with the result using the log profile likelihood method. We also applied the linear regression method with the model in Eq. (12) and obtained consistent results.

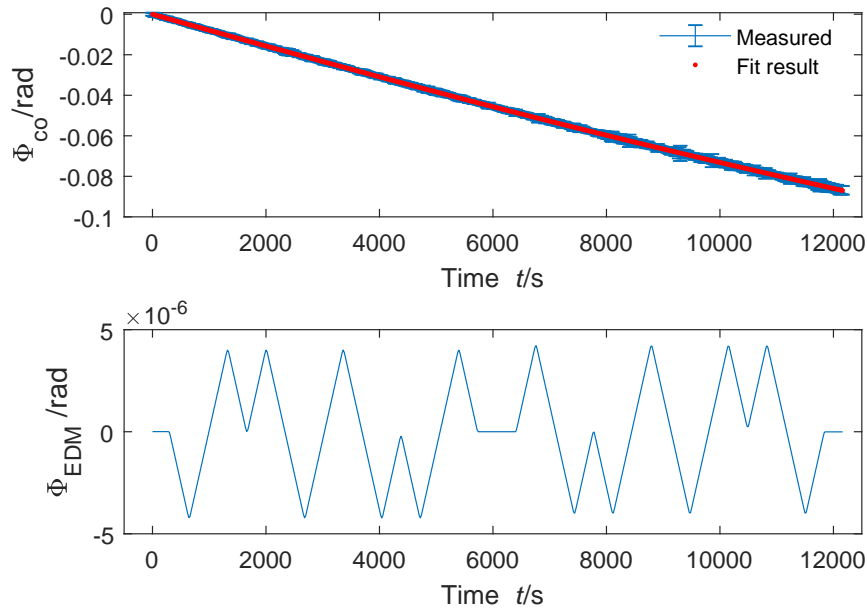


Fig. 5. The comagnetometer phase Φ_{co}^k and the data of the fit Φ_{fit}^k (top) as well as the EDM function Φ_{EDM}^k constructed from the measured electric field (bottom) with $d_h = 1 \times 10^{-27}$ e cm for the exemplary sub-run.

Table 2. Correlation matrix of the first sub-run for the fit with a 7th order polynomial and the block length $t_b=5$ s.

	a	p_0	p_1	p_2	p_3	p_4	p_5	p_6	p_7
a	1.0	0.0	0.0	0.0	0.0	0.2	0.0	0.2	0.2
p_0	0.0	1.0	0.5	0.2	0.1	0.0	0.1	0.1	0.0
p_1	0.0	0.5	1.0	0.5	0.2	0.1	0.1	0.1	0.0
p_2	0.0	0.2	0.5	1.0	0.5	0.2	0.1	0.0	0.0
p_3	0.0	0.1	0.2	0.5	1.0	0.5	0.2	0.1	0.0
p_4	0.2	0.0	0.1	0.2	0.5	1.0	0.5	0.2	0.1
p_5	0.0	0.1	0.1	0.1	0.2	0.5	1.0	0.5	0.1
p_6	0.2	0.1	0.1	0.0	0.1	0.2	0.5	1.0	0.5
p_7	0.2	0.0	0.0	0.0	0.0	0.1	0.1	0.5	1.0

3.4 The modified Allan deviation

The modified Allan deviation (MAD) is an established tool to evaluate the low-frequency drift of a time series of phases Φ , which is defined as

$$\sigma_f(\tau) = \frac{1}{2\pi} \sqrt{\frac{\sum_{j=1}^{P-3n-1} \left(\sum_{k=j}^{j+n-1} \Phi^{k+2n} - 2\Phi^{k+n} + \Phi^n \right)^2}{2n^2\tau^2(P-3n+1)}}, \quad (16)$$

where the integration time τ is n times the block length t_b , and the total measurement time T is subdivided into P time intervals of equal length τ , such that $P\tau \approx T$ [31]. As an example, the MAD of the exemplary sub-run is plotted in Fig. 6. σ_f of Φ_{co}^k reaches the minimum at the integration time τ of 550 s and then increases due to the comagnetometer frequency drift. For the residual phase $\Phi_{\text{co}}^k - \Phi_{\text{fit}}^k$ of this exemplary sub-run, the MAD decreases with increasing integration time according to $\sigma_f \propto \tau^{-3/2}$ (dashed line in Fig. 6) over the considered range, down to 0.4 nHz. This behavior is an indicator that the comagnetometer phase Φ_{co}^k is adequately described by the fit model of Eq. (12), since the residual is dominated by white phase noise.

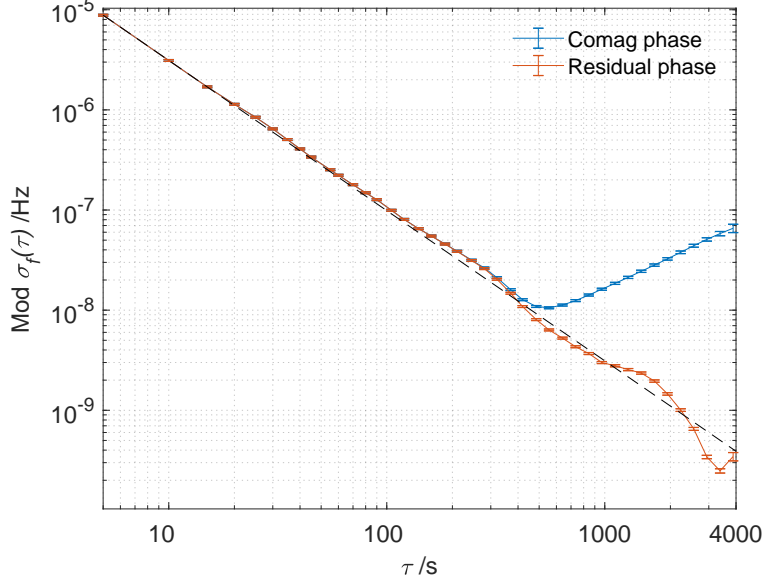


Fig. 6. The modified Allan deviation and its error bar of the accumulated comagnetometer phase and the residual phases for the fit with a 7th order polynomial. To fulfill the MAD statistics criteria [31], only data are shown for integration time $\tau < 4000$ s.

3.5 The theoretical statistical uncertainty bound

The theoretical limit of the ^{129}Xe EDM uncertainty can be derived as the CRLB, which also provides insights into optimizing experimental parameters. For the sake of simplicity, only a single species spin-precession signal is considered and its amplitude is assumed to be a constant over the whole sub-run. For the GPF method, $d_A(^{129}\text{Xe})$ is estimated with two steps: The VP fitting to obtain the phase of each block and global phase fitting of the sub-runs. Therefore, the overall CRLB is the combination of the results of these two fits.

For the phase ϕ of a sinusoid embedded in white Gaussian noise (WGN) observed over one block with time being symmetrically around 0 s, the CRLB is

$$\text{var}(\hat{\phi}) \geq \frac{2\sigma_w^2}{A^2 N}, \quad (17)$$

where σ_w^2 is the variance of the WGN, A the amplitude and N the number of data points in one block [32]. The CRLB for the parameters in the fit model Eq. (12) is the reciprocal of the Fisher information matrix

$$\mathbf{I} = \begin{pmatrix} \sum_{k=1}^{JM} \frac{(\Phi_{\text{EDM}}^k)^2}{\delta\phi_k^2} & \dots & \dots & \sum_{k=1}^{JM} \frac{\Phi_{\text{EDM}}^k t_k^g}{\delta\phi_k^2} \\ \sum_{k=1}^{JM} \frac{\Phi_{\text{EDM}}^k}{\delta\phi_k^2} & \sum_{k=1}^{JM} \frac{1}{\delta\phi_k^2} & \dots & \vdots \\ \vdots & \vdots & \ddots & \vdots \\ \sum_{k=1}^{JM} \frac{\Phi_{\text{EDM}}^k t_k^g}{\delta\phi_k^2} & \sum_{k=1}^{JM} \frac{t_k^g}{\delta\phi_k^2} & \dots & \sum_{k=1}^{JM} \frac{t_k^g t_k^g}{\delta\phi_k^2} \end{pmatrix}, \quad (18)$$

where M is the number of segments in one sub-run, and J is the number of blocks in one segment. For the sake of simplicity, the standard polynomial is used in the fit model Eq. (12). Assuming $\sum_{k=1}^{JM} \Phi_{\text{EDM}}^k t_k^i = 0$ for i going from 0 to g and the phase uncertainty $\delta\phi$ is a constant, the considered CRLB can be simplified to the so called ideal or uncorrelated CRLB as

$$\text{var}(\hat{d}_{\text{A}}(^{129}\text{Xe}))_{\text{GPF}} \geq \frac{\delta\phi^2}{\sum_{k=1}^{JM} (\Phi_{\text{EDM}}^k)^2}. \quad (19)$$

By substituting Eqs. (11), (17) and (18) into Eq. (19), and exploiting the periodic property of the constructed EDM function (see Fig. 5), for our case, $\sum_{k=1}^{JM} (\Phi_{\text{EDM}}^k)^2 = M \sum_{k=1}^J (\Phi_{\text{EDM}}^k)^2$, the overall CRLB for $d_{\text{A}}(^{129}\text{Xe})$ becomes

$$\text{var}(\hat{d}_{\text{A}}(^{129}\text{Xe}))_{\text{GPF}} \geq \frac{2\sigma_{\text{w}}^2}{A^2 N} / \left(\left(\frac{2|E|t_b}{\hbar} \right)^2 M \sum_{k=1}^J k^2 \right) \quad (20)$$

$$\geq \frac{\sigma_{\text{w}}^2}{A^2} \left(\frac{\hbar}{2|E|} \right)^2 \frac{6M^2 \delta t}{T^3}, \quad (21)$$

where $T = MJN\Delta t$ is the total measurement time and $\Delta t = 1/f_s$ is the sampling interval. Note that the number of segments M should be large enough to ensure the orthogonality between Φ_{EDM}^k and the polynomial functions. In case of an exponentially decaying amplitude A of the precession signal, the CRLB has to be calculated with Eq. (18). For the PC method, the CRLB on the ^{129}Xe EDM for M segments is derived in Ref. [26] as

$$\text{var}(\hat{d}_{\text{A}}(^{129}\text{Xe}))_{\text{PC}} \geq \frac{\sigma_{\text{w}}^2}{A^2} \left(\frac{\hbar}{2|E|} \right)^2 \frac{24M^2 \delta t}{T^3}. \quad (22)$$

The PC method applies linear fits to the comagnetometer phases within one segment to derive the comagnetometer frequency of each segment, which requires the addition of an interception term as a starting phase, increasing the variance by a factor of four compared to a linear fit without interception term. In the GPF method the accumulated comagnetometer phases within one sub-run are analyzed in a single fit, therefore the uncertainty does not increase as the interception term is orthogonal to the EDM function (see Eq. (18)). Furthermore, the PC method requires the unweighted average of at least four segment frequencies, which increases its statistical uncertainty even further.

4 Results

A Monte-Carlo study was conducted to confirm that the GPF method can reach the higher sensitivity as shown by the CRLB compared to the PC method. Later, the GPF method was used to obtain the ^{129}Xe EDM from the data set as taken in Ref. [11] using the same channel and block length for analysis. As there were data sets in the 2017 and 2018 campaigns which were not useable with the PC method but could be analyzed with the GPF method, we gathered all data and optimized the analysis parameters to obtain the minimum uncertainty from the data. Ultimately, an improved upper limit of the ^{129}Xe EDM was derived using the unblinded data.

4.1 Monte-Carlo tests

The accumulated phase of each spin species for the sampling point j was generated as

$$\Phi_{\text{Xe,syn}}^j = \int_0^{t_j} \gamma_{\text{Xe}} B(t) + 2\pi(f_{\text{lin}}^{\text{Xe}} + u^{\text{Xe}} e^{-t/T_1^{\text{Xe}}} + f_{\text{EDM}}) dt, \quad (23)$$

$$\Phi_{\text{He,syn}}^j = \int_0^{t_j} \gamma_{\text{He}} B(t) + 2\pi(f_{\text{lin}}^{\text{He}} + u^{\text{He}} e^{-t/T_1^{\text{He}}}) dt, \quad (24)$$

where the drift of the background field $B(t)$ was parametrized with a 4th order polynomial. $f_{\text{lin}}^{\text{Xe/He}}$ represent the frequency shifts caused by the chemical shift and Earth's rotation. $u^{\text{Xe/He}}$ are the drift amplitudes of the respective precession frequencies. The frequency drift was modeled as exponentially decaying functions with the characteristic time of T_1 [21, 22, 25]. Thereby it was assumed that T_1 is larger than T_2 and its range is listed in Table 3. f_{EDM} is the

frequency shift due to the coupling of a synthetic EDM d_{syn} with the electric field according to Eq. (3). Substituting Eqs. (23) and (24) into Eq. (10) results in the synthetic comagnetometer phase, whose time dependence is designed to mimic the measured data (for details see Appendix A.2). The exponentially decaying spin precession signals of ^{129}Xe and ^3He atoms can be described by

$$V_{\text{Xe/He}}^j = A_0^{\text{Xe/He}} e^{-t_j/T_2^{\text{Xe/He}}} \sin \Phi_{\text{Xe/He,syn}}^j \quad (25)$$

with $t_j = j\Delta t$, which is the time for the sampling point j .

Table 3. The range of the parameter values used for generating synthetic spin precession data for Monte-Carlo simulations.

Para.	Range	Para.	Range
u^{He}	3.5-4.5 μHz	T_1^{He}	9000-14000 s
u^{Xe}	9-11 μHz	T_1^{Xe}	9000-14000 s
$f_{\text{lin}}^{\text{He}}$	4-10 μHz	$f_{\text{lin}}^{\text{Xe}}$	4-10 μHz

The parameters used to generate synthetic data were taken from 18 sub-runs of high sensitivity from the 2018 campaign. The starting amplitude of ^{129}Xe and ^3He are set to $A_0^{\text{Xe}} = 70$ pT, $A_0^{\text{He}} = 25$ pT and $T_2^{\text{Xe/He}} = 8000$ s. The electric field contains 36 segments of 200 s up to 800 s length, as used in the measurement campaign. The values of other parameters in Eqs. (23) and (24) are random and uniformly distributed in the ranges listed in Table 3. Three different kinds of noise were separately added into the synthetic data, including two WGN with $\sigma = 154$ fT, the standard deviation of the white noise in the real data, and $\sigma = 154/5 = 30.8$ fT, as well as real SQUID gradiometer noise. The overall EDM values obtained with the GPF method from the 18 synthetic sub-runs for four synthetic values $d_{\text{syn}} = (1, 2, 5, 10) \times 10^{-28}$ e cm are plotted in Fig. 7. The averaged overall EDM uncertainty for WGN data with $\sigma = 154$ fT is 1.74×10^{-28} e cm, which is roughly a factor of 5 larger than that obtained from the data with $\sigma = 30.8$ fT and a factor of 1.1 higher than the calculated CRLB for these 18 sub-runs, which is 1.59×10^{-28} e cm. This mainly results from the correlation between the EDM and the parameters of the polynomials in the phase fit. The uncertainty for the real noise is 1.85×10^{-28} e cm, being similar to that for the white noise with $\sigma = 154$ fT. Most of the 1σ confidence intervals of the derived EDM cover the added EDM values $d_{\text{syn}} \geq 1 \times 10^{-28}$ e cm independent of the realistic noise level.

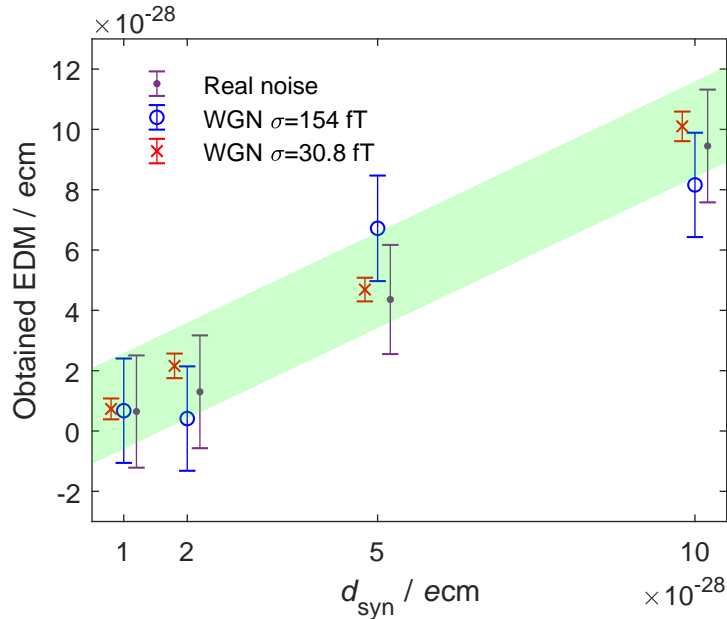


Fig. 7. The derived EDM values using the synthetic data sets. The x coordinates of the data for real noise and WGN with $\sigma = 30.6$ fT are shifted with 2×10^{-29} e cm and -2×10^{-29} e cm, respectively. The green shade illustrates the 1σ confidence interval with the added EDM as the center value and the uncertainty derived from the CRLB for $\sigma = 154$ fT.

4.2 Overall results

4.2.1 Statistical uncertainty

Applying the GPF method to the same data set of 41 runs (80 sub-runs) as analyzed by the PC method [11] and using the same channel and analysis parameters, the statistical uncertainty is decreased by a factor of 2.1 from $6.6 \times 10^{-28} e \text{ cm}$ to $3.1 \times 10^{-28} e \text{ cm}$.

Due to fewer constraints in the GPF method, runs with the number of segments $M \neq 4n$ with $n \in \mathbb{N}$ or having SQUID jumps could be included in the data analysis, leading to a total of 45 runs (87 sub-runs). Furthermore, the segments with zero high voltage are included into the analysis. For the analysis, the block length is $t_b = 5 \text{ s}$, the threshold of the F -test is set to $P_{\min} = 0.6$ (see Appendix B) and the minimum order of the polynomial used in the fit is set to 4 in order to adequately describe the comagnetometer phase drift. The average polynomial order used for all sub-runs is 6.4 and the maximum order 13.

The overall result using the full data set is $d_A(^{129}\text{Xe}) = 1.1 \pm 3.1 \times 10^{-28} e \text{ cm}$ with $\chi^2/\text{dof} = 115.5/86$. As all sub-run measurements were taken with considerable different background noise a $\chi^2/\text{dof} \geq 1$ can be expected. According to the PDG guidelines [33] we accounted for these random variations by scaling the statistical uncertainty with the factor $\sqrt{\chi^2/\text{dof}} = 1.16$ leading to $3.6 \times 10^{-28} e \text{ cm}$. Bootstrapping [34] the 87 EDM measurements resulted in an estimate of the statistical uncertainty of $3.14 \times 10^{-28} e \text{ cm}$. Fig. 8 shows the derived EDM results per sub-run. Sorting all EDM measurements into groups based on the experimental parameters, such as the cell geometry, B_0 field direction, number and duration of segments and the gas pressure, shows no correlation between the deduced EDM value and these parameters, as can be seen in Fig. 9. Furthermore, no correlation between the chosen polynomial order and the derived sub-run EDM values was seen.

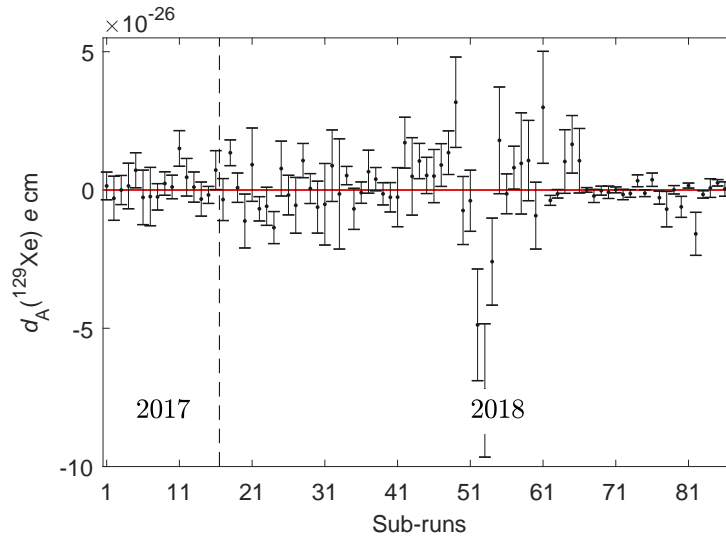


Fig. 8. EDM results of the 2017 and 2018 campaigns derived with the GPF method by sub-runs. The thin orange bar is the confidence interval of 1σ around the weighted mean. The reason for a lower uncertainty in the last 20 sub-runs is a change in the experimental parameters as explained in detail in Ref. [11].

4.2.2 Systematic uncertainty

The systematic uncertainties of the two experiment campaigns were extensively studied in Ref. [11]. We applied the same analysis to the full data set used here and the derived systematic uncertainties are summarized in Table 4. The correction to the comagnetometer frequency drift of order higher than 1, as it has been done in Ref. [11], becomes obsolete for the GPF method since the model of Eq. (12) considers the higher order drifts implicitly.

As mentioned above, the GPF uses the full data set, including data during the high voltage rampings. Therefore the charging current can have an impact on the result in two ways. First the charging current could magnetize parts of the experimental equipment, and change the magnetic field seen by the spins. By this mechanism a false EDM may be generated. This effect has been carefully analyzed in Ref. [11] and has been adapted for the data set used for GPF (see Charging current in Table 4). Secondly, the charging currents just as the leakage currents will generate magnetic

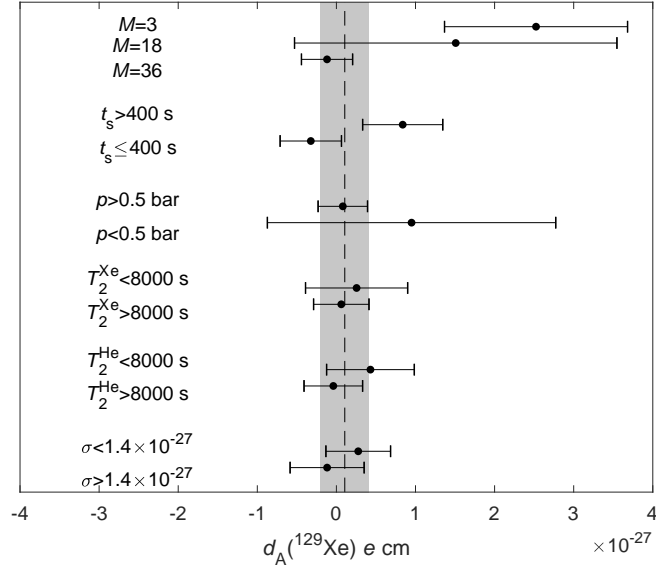


Fig. 9. The EDM results for grouping the data set by number of segments M , segment duration t_s , gas pressure p , T_2^{Xe} , T_2^{He} , and the statistical uncertainty threshold of $1.4 \times 10^{-27} e \text{ cm}$. The dashed line is at $d_A(^{129}\text{Xe}) = 1.1 \times 10^{-28} e \text{ cm}$ and the gray region indicates the confidence interval of 1σ with the unscaled statistical uncertainty. For clarity of the figure, only a few parameters are plotted here.

fields, which are correlated with the electric field direction. This effect is only present during the ramping lasting for a few blocks per segment, ranging from 20 to 160 blocks. The impact of the charging current acting as a leakage current is calculated and turned out to be negligible, relative to the effect of leakage currents as given in Table 4.

We further looked for the potential effect of the comagnetometer drift and the vibrational noise with Monte-Carlo simulations and did not find observable systematic error, see Appendix A.

Table 4. The systematic uncertainties determined as done in Ref. [11] based on the data set used for the GPF method.

	2017 ($e \text{ cm}$)	2018 ($e \text{ cm}$)
Leakage current (incl. impact of I_{Charging} during ramping)	1.2×10^{-28}	4.4×10^{-31}
Charging current	1.7×10^{-29}	1.2×10^{-29}
Cell motion (rotation)	4.2×10^{-29}	4.0×10^{-29}
Cell motion (translation)	2.6×10^{-28}	1.9×10^{-28}
$ E ^2$ effect	1.2×10^{-29}	2.2×10^{-30}
$ E $ uncertainty	9.9×10^{-29}	5.7×10^{-30}
Geometric phase	$\leq 2 \times 10^{-31}$	$\leq 1 \times 10^{-29}$
Total systematic uncertainty	3.07×10^{-28}	1.95×10^{-28}
Scaled statistical uncertainty	15.57×10^{-28}	3.67×10^{-28}

The overall systematic uncertainty is the weighted average of the systematic uncertainties of the two measurement campaigns 2017 and 2018 using the reciprocal of its statistical variance as weights, yielding $2.0 \times 10^{-28} e \text{ cm}$. The final result, separating the statistical and systematic uncertainties, is

$$d_A(^{129}\text{Xe}) = 1.1 \pm 3.6_{(\text{stat})} \pm 2.0_{(\text{syst})} \times 10^{-28} e \text{ cm}, \quad (26)$$

from which we set an upper limit $|d_A(^{129}\text{Xe})| < 8.3 \times 10^{-28} e \text{ cm}$ at the 95% C.L. This reanalysis leads to a limit that is a factor of 1.7 smaller compared to the previous result [11] and a factor of 8.0 compared to the result in 2001 [16].

5 SUMMARY AND OUTLOOK

We proposed a global phase fitting method to analyze spin precession data. Applying the GPF method to the data set used in Ref. [11] yields a consistent result for $d_A(^{129}\text{Xe})$ but a two times smaller statistical uncertainty compared to the PC method, as predicted by the theoretical CRLB analysis. Using additional data which had to be discarded for the PC method due to incomplete electric field patterns and optimizing the analysis parameters, the upper limit of the ^{129}Xe EDM improves by a factor of 1.7 to $|d_A(^{129}\text{Xe})| < 8.3 \times 10^{-28} e \text{ cm}$ at the 95% C.L. This enables ^{129}Xe to be used as a comagnetometer in future neutron EDM experiments [35] with a systematic error contribution down to $|d_A(^{129}\text{Xe})| \times \gamma_n/\gamma_{\text{Xe}} = 2.1 \times 10^{-27} e \text{ cm}$. Our GPF method relieves the demands on the physical model describing the comagnetometer frequency drift and could be generally used in similar spin precession experiments, such as the Lorentz-invariance test. By optimizing the experimental parameters for the GPF method (see Appendix C), the upper limit for $d_A(^{129}\text{Xe})$ could be reduced even further, as planned for an upcoming EDM campaign with optimized high voltage pattern.

Acknowledgements

We acknowledge the support of the Core Facility ‘Metrology of Ultra-Low Magnetic Fields’ at Physikalisch-Technische Bundesanstalt which receives funding from the Deutsche Forschungsgemeinschaft (DFG KO 5321/3-1 and TR 408/11-1). This work was supported by Deutsche Forschungsgemeinschaft grants TR408/12 and FA1456/1-1. T. Liu acknowledges the support from the Funds for International Cooperation and Exchange of the National Natural Science Foundation of China (grant number 51861135308). We gratefully thank Dr. U. Steinhoff and Dr. G. Wübbeler for fruitful discussion.

Authors contributions

All the authors collaborated in the same way in the ideas, development and writing of the manuscript.

A EXPERIMENT DEPENDENT FACTORS

Here we applied Monte-Carlo simulation to investigate the impact of two non-ideal factors on the derived EDM result, namely the vibrational noise and the comagnetometer phase drift.

A.1 Vibrational noise

The effect of the real measurement noise (e.g. vibrational noise) on the estimated phase is quantitatively analyzed. Here, synthetic data is generated, using a single sinusoidal function with a constant amplitude $A = 30 \text{ pT}$, with a length of 10000 s yielding 2000 blocks. Furthermore, white noise with $\sigma = 154 \text{ fT}$ (the standard deviation of the white noise in real gradiometer data) generated with MATLAB, or real noise (from the exemplary sub-run with a total noise power of 0.4 pT and the precession signals filtered out) were added separately to the synthetic data. The error of the fitted phase for block i is defined as $\epsilon_i = \phi_{\text{fit},i} - \phi_{\text{real},i}$. Here $\phi_{\text{real},i}$ is known and $\phi_{\text{fit},i}$ is obtained from the fit to block i .

The histograms of ϵ_i for these two synthetic data sets are plotted in Fig. 10. The error for the white noise data is in good agreement with the normal distribution with $\sigma = 1.11 \times 10^{-4} \text{ rad}$, which is close to $1.08 \times 10^{-4} \text{ rad}$, the CRLB on the phase estimator in Eq. (17). The error for the real noise data also satisfies the Gaussian distribution, with a similar result as the white noise data. This implies that the vibrational noise did not cause evident additional phase deviation, although the standard deviation of the vibrational noise is around 7 times bigger than the white noise. As evident in Fig. 10, the vibrational noise does not cause an observable systematic error on the derived phase.

A.2 Comagnetometer phase drift

The analyzed comagnetometer phase drift Φ_{co}^k for 9 sub-runs with high sensitivities on ^{129}Xe EDM are plotted in the left panel of Fig. 11. Note that the linear drifts due to Earth’s rotation and chemical shift were subtracted by using the deterministic equations [17]. The synthetic comagnetometer phase drifts generated with two exponential functions for 18 random sub-runs are plotted in the right panel of Fig. 11, showing a similar behavior as the experimentally obtained ones. The parameter ranges are listed in Table 3.

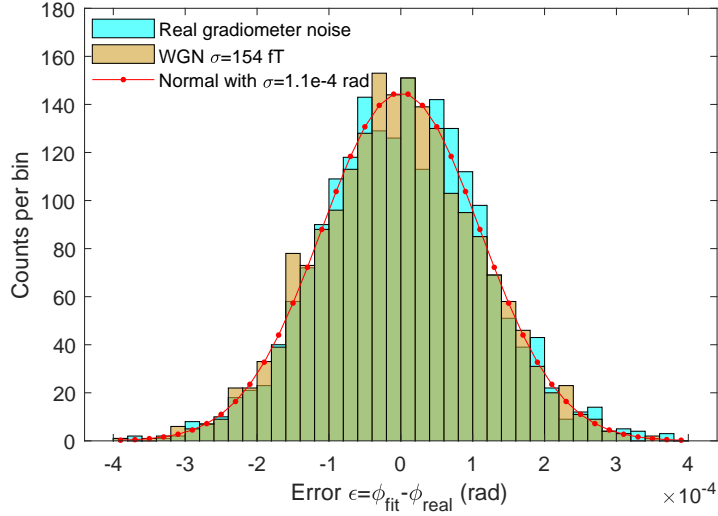


Fig. 10. Histograms of the phase error from the synthetic data with real gradiometer noise (light blue) and white noise (yellow). The data lasts for 10 000 s and consists of 200 blocks.

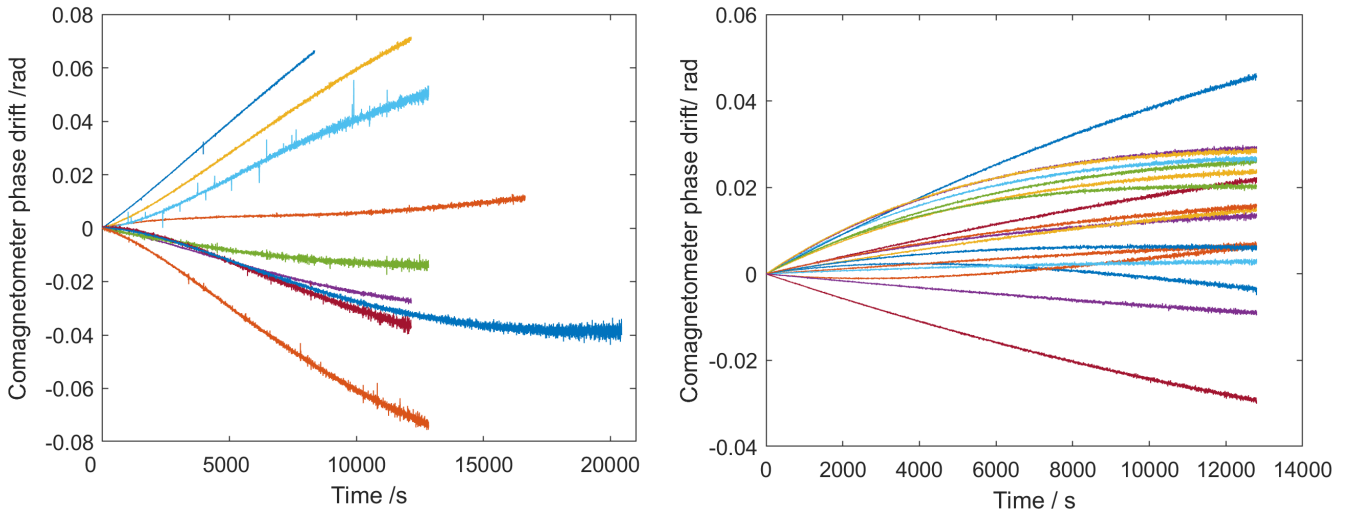


Fig. 11. Left: Measured comagnetometer phase drift of 9 sub-runs reduced by the linear deterministic term stemming from the Earth’s rotation and chemical shift. The green curve is the result of the exemplary sub-run used in Sec. 3. Right: synthetic data of 18 sub-runs.

To investigate the potential systematic effect caused by the comagnetometer phase drift, we altered the drift amplitude u^{Xe} and u^{He} in Eqs. (23) and (24) in the synthetic phase data. Fig. 12 shows the derived EDM values as a function of the scale ratio of the drift amplitude. No distinct correlation between the obtained EDM value and the drift amplitude could be observed. Therefore, we did not assign a model dependent uncertainty for the comagnetometer drift when applying the GPF method.

B THE F -TEST THRESHOLD

The F -test threshold P_{\min} affects the polynomial order used in the GPF method, as listed in Table 5. The EDM values for various P_{\min} are overlapped within the 1σ statistical uncertainty and are all consistent with zero. Additionally, the upper limit of the ^{129}Xe EDM is almost insensitive to the threshold. We have chosen 0.6 as F -test threshold yielding the highest upper bound.

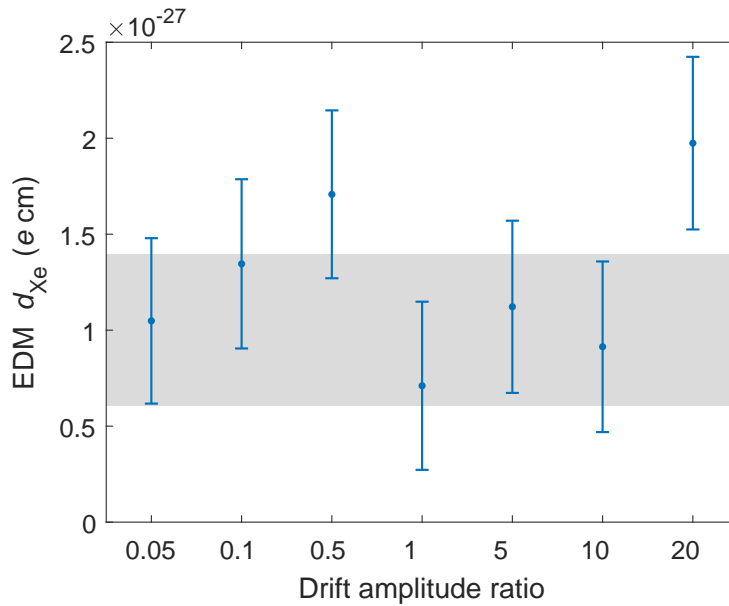


Fig. 12. The derived EDM value as a function of the scale ratio of the drift amplitude to the observed drift in two campaigns. The uncertainty is for 1σ . Each result is an average of 40 sub-runs lasting 12800 s and with 32 high voltage segments. The gray bar indicates the 1σ confidence interval with the added EDM as the center value and the uncertainty derived from the CRLB.

Table 5. The overall EDM results with various F -test threshold P_{\min} .

P_{\min}	Average order	EDM ($10^{-28} e \text{ cm}$)	Uncertainty ($10^{-28} e \text{ cm}$)	Reduced χ^2	P -value	Upper limit (95% C.L.) ($10^{-28} e \text{ cm}$)
0.4	8.2	0.08	3.22	1.32	0.03	8.2
0.5	7.3	-0.36	3.20	1.24	0.06	8.0
0.6	6.4	1.06	3.08	1.34	0.02	8.3
0.7	6.0	-0.07	3.06	1.26	0.05	7.8
0.8	5.5	-0.87	3.05	1.31	0.03	8.1

C DESIGN OF EXPERIMENTAL PARAMETERS

The number of segments M in one sub-run has a significant impact on the estimation uncertainty derived by the GPF method. According to the ideal CRLB, a smaller number of segments results in a lower uncertainty, shown as the red line in Fig. 13. To search for the optimum segment number, we used the synthetic comagnetometer phase data with added white Gaussian noise. The phase uncertainty increases with time and starts with 0.1 mrad. The time constants T_2 for ^{129}Xe atoms and ^3He atoms are a random number ranged from 8000 s to 9000 s. The total measurement time length is fixed to 38400 s, while M is varied from 2 to 64. The averaged EDM value over 100 runs for each M are plotted as the blue crosses. The fit uncertainty is larger than the ideal CRLB due to the correlation between the EDM function and the phase drift. The gap is reduced with the increase of M , since the orthogonality condition is satisfied better. A relatively flat optimum is found around $M = 16$. Note that this optimum value also depends on the total measurement time. A sub-run with longer measurement time calls for a higher number of segments, hence the optimum number for $T = 6400$ s and $T = 64000$ s is 8 and 64, respectively. The improved understanding of the comagnetometer frequency drift behavior may reduce the requirement on the segment number, thus significantly increasing the measurement sensitivity.

References

- [1] Andrei D. Sakharov. “Violation of CP in variance, C asymmetry, and baryon asymmetry of the universe”. *JETP Letters* 5.5 (1967), pp. 24–27.
- [2] Laurent Canetti, Marco Drewes, and Mikhail Shaposhnikov. “Matter and antimatter in the universe”. *New Journal of Physics* 14.9 (2012), p. 095012.

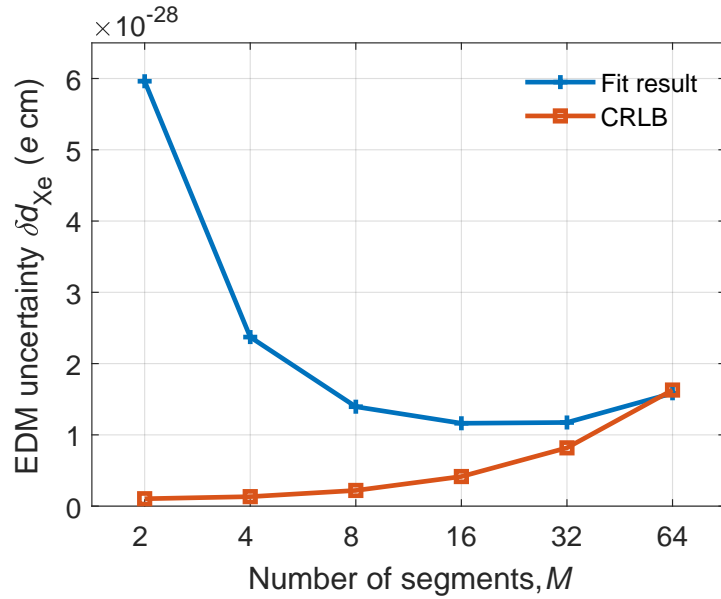


Fig. 13. The averaged EDM value over 100 random simulated runs. The reduced chi-square value was normalized to 1 for each result. The solid lines are guides for the eye.

- [3] Michael Dine and Alexander Kusenko. “Origin of the matter-antimatter asymmetry”. *Reviews of Modern Physics* 76.1 (2003), pp. 1–30.
- [4] T. E. Chupp, P Fierlinger, M. J. Ramsey-Musolf, and J. T. Singh. “Electric dipole moments of atoms, molecules, nuclei, and particles”. *Reviews of Modern Physics* 91.1 (2019), p. 015001.
- [5] William B. Cairncross and Jun Ye. “Atoms and molecules in the search for time-reversal symmetry violation”. *Nature Reviews Physics* 1.8 (2019), pp. 510–521.
- [6] J. H. Smith, E. M. Purcell, and N. F. Ramsey. “Experimental Limit to the Electric Dipole Moment of the Neutron”. *Physical Review* 108.1 (1957), pp. 120–122.
- [7] V. V. Flambaum, M. Pospelov, A. Ritz, and Y. V. Stadnik. “Sensitivity of EDM experiments in paramagnetic atoms and molecules to hadronic CP violation”. *Physical Review D* 102.3 (2020), p. 035001.
- [8] B. Graner, Y. Chen, E. G. Lindahl, and B. R. Heckel. “Reduced Limit on the Permanent Electric Dipole Moment of ^{199}Hg ”. *Physical Review Letters* 116.16 (2016), pp. 1–5.
- [9] Akitada Sakurai, B K Sahoo, K Asahi, and B P Das. “Relativistic many-body theory of the electric dipole moment of ^{129}Xe and its implications for probing new physics beyond the standard model”. *Physical Review A* 100.2 (2019), p. 020502.
- [10] Michael Bishof et al. “Improved limit on the ^{225}Ra electric dipole moment”. *Physical Review C* 94.2 (2016), pp. 1–17.
- [11] N. Sachdeva et al. “New Limit on the Permanent Electric Dipole Moment of ^{129}Xe Using ^3He Comagnetometry and SQUID Detection”. *Physical Review Letters* 123.14 (2019), p. 143003.
- [12] D. Cho, K. Sangster, and E. A. Hinds. “Tenfold improvement of limits on T violation in thallium fluoride”. *Physical Review Letters* 63.23 (1989), pp. 2559–2562.
- [13] C Abel et al. “Measurement of the Permanent Electric Dipole Moment of the Neutron”. *Physical Review Letters* 124.8 (2020), p. 081803.
- [14] C. A. Baker et al. “Improved Experimental Limit on the Electric Dipole Moment of the Neutron”. *Physical Review Letters* 97.13 (2006), p. 131801.
- [15] F. Allmendinger, I. Engin, W. Heil, S. Karpuk, H.-J. Krause, B. Niederländer, A. Offenhäusser, M. Repetto, U. Schmidt, and S. Zimmer. “Measurement of the permanent electric dipole moment of the ^{129}Xe atom”. *Physical Review A* 100.2 (2019), p. 022505.
- [16] M. A. Rosenberry and T. E. Chupp. “Atomic Electric Dipole Moment Measurement Using Spin Exchange Pumped Masers of ^{129}Xe and ^3He ”. *Physical Review Letters* 86.1 (2001), pp. 22–25.
- [17] C. Gemmel et al. “Ultra-sensitive magnetometry based on free precession of nuclear spins”. *European Physical Journal D* 57.3 (2010), pp. 303–320.
- [18] F. Allmendinger, W. Heil, S. Karpuk, W. Kilian, A. Scharth, U. Schmidt, A. Schnabel, Yu Sobolev, and K. Tullney. “New Limit on Lorentz-Invariance- and CPT-Violating Neutron Spin Interactions Using a Free-Spin-Precession ^3He - ^{129}Xe Comagnetometer”. *Physical Review Letters* 112.11 (2014), pp. 1–5.

- [19] F. Allmendinger, U. Schmidt, W. Heil, S. Karpuk, A. Scharth, Yu Sobolev, and K. Tullney. “Allmendinger et al. Reply:” *Physical Review Letters* 113.18 (2014), p. 188902.
- [20] Michael V. Romalis, Dong Sheng, Brian Saam, and Thad G. Walker. “Comment on New Limit on Lorentz-Invariance- and CPT-Violating Neutron Spin Interactions Using a Free-Spin-Precession ^3He - ^{129}Xe Comagnetometer”. *Physical Review Letters* 113.18 (2014), p. 188901.
- [21] M E Limes, N Dural, M V Romalis, E. L. Foley, T. W. Kornack, A. Nelson, L. R. Grisham, and J. Vaara. “Dipolar and scalar ^3He - ^{129}Xe frequency shifts in stemless cells”. *Physical Review A* 100.1 (2019), p. 010501.
- [22] W. A. Terrano, Jonas Meinel, Natasha Sachdeva, T. E. Chupp, Skyler Degenkolb, Peter Fierlinger, Florian Kuchler, and Jaideep T. Singh. “Frequency shifts in noble-gas comagnetometers”. *Physical Review A* 100.1 (2019), p. 012502.
- [23] R. Golub and S. K. Lamoreaux. “Neutron electric-dipole moment, ultracold neutrons and polarized ^3He ”. *Physics Reports* 237.1 (1994), pp. 1–62.
- [24] V. V. Flambaum and A. Kozlov. “Extension of the Schiff theorem to ions and molecules”. *Physical Review A* 85.2 (2012), pp. 1–7.
- [25] D. A. Thrasher, S. S. Sorensen, J. Weber, M. Bulatowicz, A. Korver, M. Larsen, and T. G. Walker. “Continuous comagnetometry using transversely polarized Xe isotopes”. *Physical Review A* 100.6 (2019), p. 061403.
- [26] Natasha Sachdeva. “A Measurement of the Permanent Electric Dipole Moment of ^{129}Xe ”. PhD thesis. The University of Michigan, 2019.
- [27] Gene Golub and Victor Pereyra. “Separable nonlinear least squares: the variable projection method and its applications”. *Inverse Problems* 19.2 (2003), R1–R26.
- [28] K. Tullney et al. “Constraints on spin-dependent short-range interaction between nucleons”. *Physical Review Letters* 111.10 (2013), p. 100801.
- [29] Refaat El Attar. *Legendre Polynomials And Functions*. South Carolina: CreateSpace Independent Publishing Platform, 2009.
- [30] Philip R. Bevington and D. Keith Robinson. *Data Reduction and Error Analysis for the Physical Sciences*. Vol. 7. 4. McGraw-Hill, 1992, p. 415.
- [31] D.W. Allan and J.A. Barnes. “A Modified ”Allan Variance” with Increased Oscillator Characterization Ability”. Ed. by Thirty Fifth Annual Frequency Control Symposium. Philadelphia, Pennsylvania, USA, IEEE, 1981, pp. 470–475.
- [32] STEVEN M. KAY. *Fundamentals of Statistical Signal Processing, Volume I: Estimation Theory*. New Jersey: Prentice Hall PTR, 1993, p. 57.
- [33] J. Beringer et al. “Review of Particle Physics”. *Physical Review D* 86.1 (2012), p. 010001.
- [34] Bradley Efron. *The jackknife, the bootstrap, and other resampling plans*. Philadelphia: Society for Industrial and Applied Mathematics, 1982.
- [35] Yasuhiro Masuda, Koichiro Asahi, Kichiji Hatanaka, Sun Chan Jeong, Shinsuke Kawasaki, Ryohei Matsumiya, Kensaku Matsuta, Mototsugu Mihara, and Yutaka Watanabe. “Neutron electric dipole moment measurement with a buffer gas comagnetometer”. *Physics Letters, Section A: General, Atomic and Solid State Physics* 376.16 (2012), pp. 1347–1351.